Optics Communications 315 (2014) 138–146

Contents lists available at ScienceDirect

Optics Communications

journal homepage: www.elsevier.com/locate/optcom

Ultra-compact low-voltage and slow-light MZI electro-optic modulator based on monolithically integrated photonic crystal

Yanhong Zhang [a], Huiping Tian [a,*], Daquan Yang [a], HongZhan Liu [a,b], Yuanyuan Liu [c], Yuefeng Ji [a]

[a] The State Key Laboratory of Information Photonics and Optical Communications, School of Information and Telecommunication Engineering, Beijing University of Posts and Telecommunications, Beijing 100876, China
[b] Laboratory of Nanophotonic Functional Materials and Devices, South China Normal University, Guangzhou 510006, China
[c] Institute of Semiconductors, Chinese Academy of Science, Engineering Research Center for Semiconductor Integrated Technology, China

ARTICLE INFO

Article history:
Received 6 June 2013
Received in revised form
22 July 2013
Accepted 5 October 2013
Available online 29 October 2013

Keywords:
Photonic crystal
Modulation
Waveguide
Optical integration

ABSTRACT

In this paper, we study an ultra-compact slow-light MZI electro-optic modulator with low voltage and high modulation bandwidth by simulation. The proposed device is totally based on monolithic integrated lithium niobate ($LiNbO_3$) photonic crystal (PC). A slow light line defect waveguide forms the interaction region. The splitter–combiner with high transmission consists of a PC Y-junction and two 60° bends. Meanwhile, with a step PC taper we significantly enhance the coupling to the slow light mode. And we finally realize an integrated modulator embedded in a monolithic photonic crystal. The whole length of the device is 91.59 μm, the half-wave drive voltage is as small as 0.66 V and the high modulation bandwidth can achieve up to 100 GHz in theory. Besides, the modulator covers over 22.3 nm optical bandwidth at telecom wavelength range.

1. Introduction

Recently, MZI electro-optic modulators with low driving voltage and compact size have become a subject of intense interest because they offer a principal component required in some optical communication systems, such as the on-chip optical interconnect system and the Radio-over-Fiber (RoF) transmission system [1,2]. In the past few years, numerous different architectures have been developed, including silicon optical modulators, based on free carrier plasma dispersion effect on pn or pin junctions [3,4], silicon-organic hybrid (SOH) electro-optic modulators [5–7], modulators based on carrier depletion effect [8–10], and $LiNbO_3$ electro-optical modulator [11–13] based on electro-optical effect. And today's state-of-the-art technology for electro-optic modulator is based on rib waveguide [11–14]. Meanwhile, electro-optic modulators based on photonic crystal (PC) are particularly interesting. For example, Nguyen et al. developed a photonic crystal modulator consisting of a 200 μm-long photonic crystal waveguide. The modulator is with an embedded p–n junction and incorporated into an asymmetric Mach–Zehnder interferometer which is based on rib waveguide [15]. Brosi et al. demonstrated a modulator with a drive voltage of 1 V, length of 80 μm and bandwidth of 78 GHz, which was based on a polymer-infiltrated photonic crystal slot waveguide [16]. And Wang et al. proposed an electro-optic modulator with a drive voltage of 1.25 V, a bandwidth of 100 GHz and a size of 42.6 μm, which was based on a $LiNbO_3$ slow light photonic crystal waveguide [17].

However, these architectures could not combine ultra-compact size, low driving voltage, and high modulation bandwidth on an ultra-compact integrated chip. Although they designed devices which can achieve low driving voltage and high-speed modulation [17,18], they are just partly based on photonic crystal. And the combiner and splitter of above mentioned devices consist of rib waveguides, which limits the integrated system relied on photonic crystal. However, many devices are totally based on monolithic photonic crystal [17–20]. In addition, high transmission of 60° bends and branches based on photonic crystal hs been proposed [21–23]. As a result, it is possible to achieve an ultra-compact MZI electro-optic modulator on a monolithic photonic crystal slab. And this modulator is easier to be utilized in integrated circuits with ultra-compact size and high performance. What is more, there have been some experimental demonstrations on the proposed $LiNbO_3$ photonic crystal [24,25], which illustrate the feasibility of building photonic crystal devices with $LiNbO_3$.

In this paper, we theoretically study an ultra-compact integrated photonic crystal Mach–Zehnder interferometer (MZI) electro-optic modulator based on a monolithic lithium niobate ($LiNbO_3$).

* Correspondence to: P.O. Box 90, BUPT, No. 10, Xitucheng Road, Haidian District, 100876 Beijing, PR China. Tel.: +86 10 61198422x605; fax: +86 10 61198422x616.
E-mail addresses: hptian@bupt.edu.cn (H. Tian), jyf@bupt.edu.cn (Y. Ji).

0030-4018/$ - see front matter © 2013 Elsevier B.V. All rights reserved.
http://dx.doi.org/10.1016/j.optcom.2013.10.020

The modulator can cover over 22.3 nm optical bandwidth at telecom wavelength range (~ 1550 nm). And it has a modulation bandwidth of 100 GHz, a drive voltage of 0.66 V and a total size of only 91.59 μm. For this design, the high linear electro-optic coefficient of $LiNbO_3$ is utilized to combine with the slow light photonic crystal waveguide. Meanwhile, Y-junctions and 60° bends are used for splitter and combiner on the same slab. In order to enhance the coupling efficiency to the slow light mode, a step taper is demonstrated between the slow light waveguide and the splitter. And there is also one taper between the slow light waveguide and the combiner. The MZI modulator can be widely employed in on-chip optical interconnect applications and integrated devices especially those based on photonic crystal.

2. PC integrated MZI modulator structure

The schematic of the proposed MZI modulator based on lithium niobate ($LiNbO_3$) is shown in Fig. 1. As is shown in Fig. 1, the modulator based on a monolithic photonic crystal consists of three parts: splitter, slow light waveguides and combiner. All of them are fabricated on the same $LiNbO_3$ slab with air holes etched. The total length of the modulator is L_1+2L_2. Both splitter and combiner are based on the integration of a Y-junction and waveguide bend. Both arms of the MZI are composed of slow light line detect waveguides of length L_1. There are three metallic electrodes (shadowed region) at the edge of the slow light waveguides. These three metallic electrodes are parallel to the slow light waveguides and the high electro-optical effect of $LiNbO_3$ is employed. Both outer electrodes are grounded and a modulating voltage U applied to the center electrode generates a voltage wave. The incident light is TE polarized. In each arm, the electric modulator field $E_{el}=U/d$ is dominantly oriented along the Z-direction. The strategy of optimization of the modulator will be analyzed in the following sections.

3. Modulating theory

Due to the Pockels effect, an external voltage can lead to refractive index change. Namely, the variation relates to the second-order susceptibility $\chi^{(2)}$ which can be calculated as [17]

$$\Delta n=-\frac{n_{LN}^3\gamma_{33}U}{2d} \tag{1}$$

where n_{LN} is an extraordinary refractive index, γ_{33} represents the nonlinear electro-optical coefficient, U refers to the applied modulating voltage, and d means the distance between electrodes. Furthermore, there is a great enhancement of the nonlinear effects

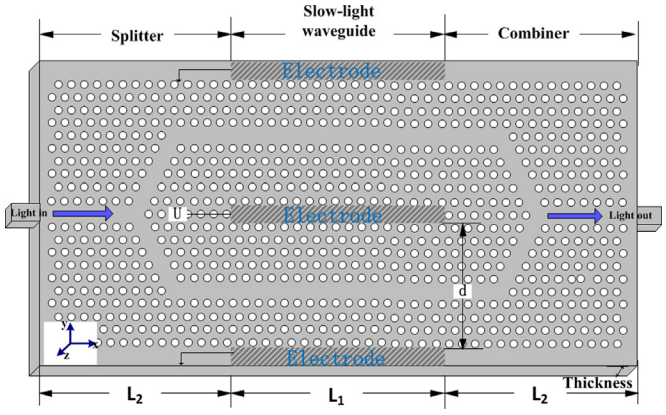

Fig. 1. The schematic of MZI modulator based on $LiNbO_3$ photonic crystal.

in system with slow light because of the compression of local density of states. Taking the effect of the second-order susceptibility caused by nano-structuring into consideration, the effective susceptibility in slow light structured materials can be expressed as [26,27]

$$\chi_{PC}^{(2)}=f_1f_2f_3\chi_{BULK}^{(2)} \tag{2}$$

where $\chi_{PC}^{(2)}$ is the second-order susceptibility of the slow light structured materials, f_i $(i=1,3)$ is the local factor for the three waves in the second order process, $\chi_{BULK}^{(2)}$ means the second-order susceptibility of bulk materials. Thus, the electro-optic coefficient becomes $f_1f_2f_3\gamma_{33}$ and Eq. (1) becomes

$$\Delta n=-\frac{n_{LN}^3f_1f_2f_3\gamma_{33}U}{2d} \tag{3}$$

Indeed, taking the local field factor into consideration, expression (3) becomes [28,29]

$$\Delta n=-\frac{n_{LN}^3f_{opt}^2f_{el}\gamma_{33}U}{2d} \tag{4}$$

where f_{opt} and f_{el} are the local optical field and the local electrical field factor. According to [28,29], the local electrical field factor is quite similar to the local optical field. In other words, we can assume $f_{opt}\approx f_{el}$. And expression (4) becomes

$$\Delta n=-\frac{n_{LN}^3f_{opt}^3\gamma_{33}U}{2d} \tag{5}$$

And the theory has been demonstrated experimentally in some papers [30–32]. The local optical field factor in the photonic crystals can be calculated as [30–32]

$$f_{opt}=\sqrt{\frac{v_g^{BULK}}{v_g^{PC}}} \tag{6}$$

where the group velocity v_g^{BULK} is in the bulk substrate and v_g^{PC} means the group velocity in the photonic crystals structure. The total phase shift of the optical wave due to the index change in slow light waveguide of length L_1 can be calculated as [17]

$$\Delta\varphi=-\Delta nk_0L_1 \tag{7}$$

where $k_0=2\pi f_0/c$ is the vacuum wavenumber, L_1 is the length of the slow light waveguide section. In this paper f_0 is settled at 193.55 THz. In order to achieve the change of $\Delta\varphi=\pi$ within the length L_1, a π-Voltage defined U_π is required. U_π is key parameter for a MZI modulator's sensitivity According to Eqs. (3)–(5), U_π can be computed as [16,17]

$$U_\pi=\frac{cd}{n_{LN}^3f_0\gamma_{33}L_1{f_{opt}}^3} \tag{8}$$

Considering the walk-off between electrical and optical waves which limits the bandwidth of MZI, it is more favorable to configure the structure ignoring terminating resistance to make the MZI modulator simple. Therefore, the $f_{3\ dB}$ can be expressed as [16,17]

$$f_{3\ dB}=\frac{0.556v_{g,opt}}{L_1(1+v_{g,opt}/v_{g,el})} \tag{9}$$

where $v_{g,opt}$ and $v_{g,el}$ mean the group velocities of the electrical waves and optical waves respectively. As $v_g=c/n_g$, Eq. (9) becomes

$$f_{3\ dB}=\frac{0.556c}{n_{g,opt}L_1(1+n_{g,el}/n_{g,opt})} \tag{10}$$

Depending on the above analysis, a triangular lattice PC slab consisting of circular air holes with lattice constant a in a dielectric $LiNbO_3$ background is assumed as the basic structure. And the

analysis provides us an important way to optimize the MZI modulator of high performance.

4. The analysis of MZI modulator

With the configuration of the MZI modulator based on lithium niobate ($LiNbO_3$) having been shown schematically in Fig. 1, here we will analyze the MZI modulator in detail. The MZI modulator is fabricated on a monolithic photonic crystal. The radius $r=0.32a$ where $a=654$ nm is the lattice constant and the slab thickness is $h=362$ nm. We take advantage of the slow light waveguide of high nonlinear effect to achieve a low π-Voltage, a broad modulation bandwidth $f_{3\ dB}$. And a 1×2 splitter and 2×1 combiner based on photonic crystal are fabricated to match the slow light section of the MZI modulator. Thus it is easy for the MZI to apply in on-chip integration especially for all those based on photonic crystal because of its compact size and high performance. However, there exists a trade-off between the frequency and bandwidth and the group index because of signal distortion, which is caused by the large group velocity dispersion and high order dispersion in the slow light regime of PC waveguide. Meanwhile, the feedback effect would reduce the transmittance of the splitter and combiner without any optimization. And in the slow light region, coupling into the slow light waveguide is inefficient due to a large impedance mismatch at boundaries of the waveguide which is caused by the large difference of group index. It is all of these factors that limit the performance of the MZI modulator.

So far there are various solutions to realize wide flat-band and high group index of slow light, i.e., using coupled waveguide [33] and modifying the position or radii of the air holes [34,35]. And varieties of structures have been demonstrated using photonic crystals, for instance, Y-junctions [36,37] and multi-mode interference splitter [38]. At the same time, various tapers have been studied to increase the coupling efficiency [39–41]. In our design, we firstly design the slow light waveguides via the method of modifying the position of the air holes. And then we design the splitter–combiner to match the slow light waveguide with the purpose of improving the performance of the monolithic MZI modulator. Thirdly we design a step taper to enhance coupling of the slow light mode in order to optimize the transmission of the modulator. The design strategy will be discussed in details in the following sections.

4.1. Design of the slow light waveguide

As is shown in Fig. 2, the waveguide is formed by omitting one line of the holes in the perfect PC. The bulk hole's radius of PCW is $r=0.32a$ and the slab thickness is $h=362$ nm. There have been kinds of means to design the slow light waveguide [33–35], but we chose the way where the first row holes are displaced symmetrically about the waveguide axis, which is easy for fabrication. The displacements relative to the unmodified lattice (red lines) are given by $S1$, where shifts towards the waveguide center are defined to be positive. The numerical simulations are supported by the plane wave expansion method using the commercial software Rsoft.

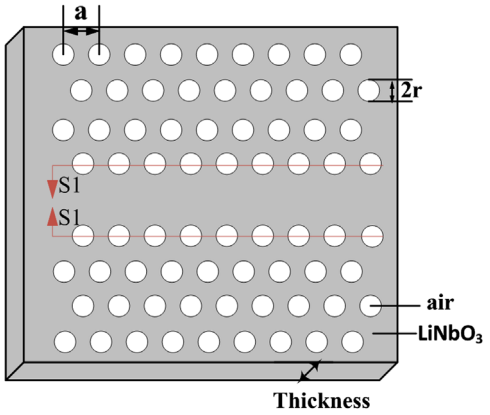

Fig. 2. Schematic configuration of slow light waveguide.

Fig. 3(a) shows the complete TE propagation information for the perfect PC waveguide. It is clear that there exists a bandgap between 0.39 and 0.46 below the light line. Fig. 3(b) presents the photonic bands of the main propagation mode (blue line) of the signal line defect PC waveguide when the polarization is assumed to be TE-like using the plane wave expansion method with $S1=0$. As is shown in Fig. 3, the PCW supports a lossless even mode. And we focus on the even mode for our numerical calculation. However, without dispersion optimization, the slow light in the $LiNbO_3$ waveguide will suffer large group velocity dispersion that causes signal distortion, which seriously affects the performance of the photonic crystals in optical interconnect applications. It is of great significance to appropriately adjust the first row of holes adjacent to the defect in order to generate a flat low group velocity dispersion region.

Fig. 4 shows how the group velocity dispersion region changes while adjusting the position of the first row of the air holes. As a result of the design process, we obtain a set of slow light waveguides which supports a low group velocity over a flat group velocity dispersion region. We found out that an increase of $S1$ decreases the group velocity, while a flat dispersion is guaranteed. For the values $S1=0.05a$, $S1=0.1a$, $S1=0.03a$, $S1=-0.03a$, and $S1=-0.05a$, the group indices n_g ($\pm10\%$) are 17, 27.5, 37, 44, and 45, respectively, while the slow light bandwidth W are 29.6 nm, 22.3 nm, 15.1 nm, 11.6 nm, and 8.0 nm respectively. The simulation results are shown in Table 1 in summary. With the purpose of avoiding having different MZI modulators to operate at each optical wavelength, it is necessary to maintain slow light waveguide coverage over a large optical bandwidth. So we choose the $n_g=27.5$ along with the bandwidth of 22.3 nm which is clearly shown by the red line in Fig. 4. That is to say, we need to design a splitter–combiner that covers $1539.4-1561.7$ nm so that the whole MZI structure can work well.

4.2. Design of the splitter–combiner

As we know about the slow light waveguides section, it is necessary to achieve a splitter–combiner which can cover $1539.4-1561.7$ nm at least with high transmission. In order to make the two sections to integrate well, we finally theoretically investigate the structure by air hole-array based on $LiNbO_3$ photonic crystal slab with $r=0.32a$. The configuration of the splitter–combiner is shown schematically in Fig. 5. The splitter–combiner is comprised of a Y-junction and two 60° waveguide bends with regular holes placed in a triangular lattice in detail. When the light is input from port 1, the structure works as a 1×2 power splitter. And the designed structure acts as a 2×1 power combiner with the light input from ports 2 and 3.

There have been different approaches to improve the performance of the bends and branches, including the coupled-mode theory [42], introducing a defect in the waveguide channel and using a heterostructure [43]. Here the radius and position are chosen as the available strategy that has proved sufficient for our purpose. There are many possible choices for which holes radii and position are allowed to be varied. And in this paper, we pick the numbered holes representing the holes whose radius or position are varied, as shown in Fig. 5. Owing to symmetry, only half of the structure needs to be optimized.

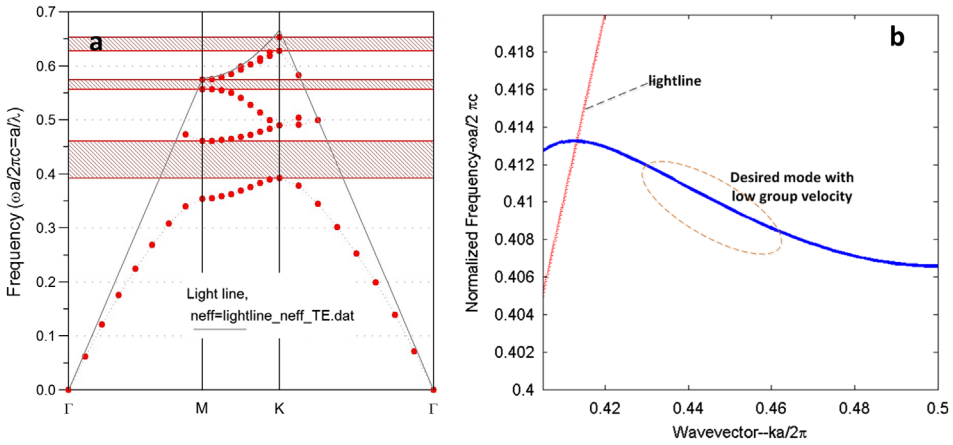

Fig. 3. (a) The computed band diagram for the perfect $LiNbO_3$ photonic crystal structure. (b) The computed band diagram for the W1 $LiNbO_3$ photonic crystal waveguide.

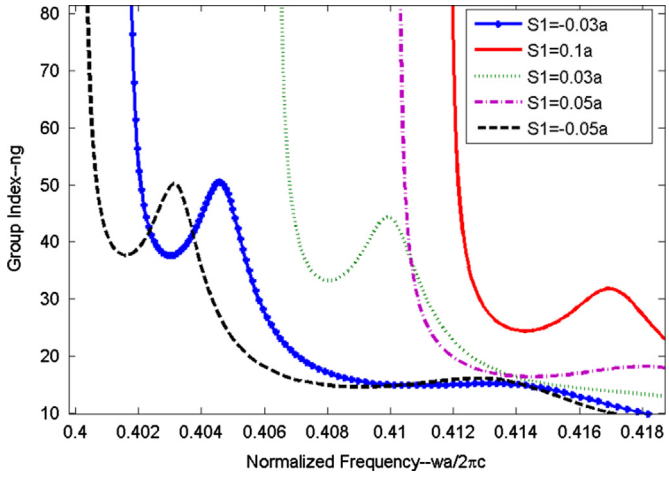

Fig. 4. Group index n_g characteristics of PC waveguide while adjusting the position of the first row of the air holes adjacent to the waveguide.

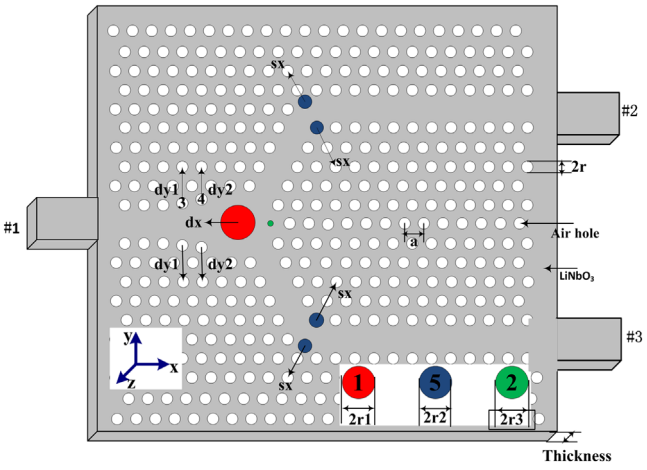

Fig. 5. Schematic of the optimized PC splitter–combiner.

Table 1
Characteristic data for a PC slow light waveguide.

a (nm)	$S1$ (a)	n_g	W (nm)	Wavelength range (nm)
646	0.05	17	29.6	1534.4–1564.1
654	0.1	27.5	22.3	1539.4–1561.7
634	0.03	37	15.1	1542.6–1557.8
627	−0.03	44	11.6	1548.1–1559.7
623	−0.05	45	8.0	1545.9–1553.9

We investigate the transmission of the splitter–combiner with different parameters of the numbered holes using the finite-different time-domain (FDTD). The simulation result is shown in Fig. 6. Fig. 6(a) shows the transmission spectrum of the structure functioning as splitter via placing the source and monitor at ports 1 and 2 respectively. And as is shown in Fig. 6(b), the transmission spectrum of the structure operating as combiner is achieved by placing the source and monitor at ports 2 and 1. As Fig. 6 shows, the parameters of the numbered holes have a serious impact on the performance of the splitter–combiner. With a careful design, we can conclude that the structure has a high transmission over the desired wavelength range when the parameters of the numbered holes are fixed at $r1=0.7a$, $r2=0.2a$, $r5=0.4a$, $sx=0.16a$, $dy1=0.1a$, and $dy2=0.2a$.

The transmission spectrum of the optimized photonic crystal splitter–combiner is shown clearly by the red line in Fig. 6. As shown in Fig. 6(a), we can find the structure is of high transmission over 40% (each output) and covers a desired transmission region which is signed yellow, when the structure is for splitting. Meanwhile, in Fig. 6(b), we find out if the structure acts as a combiner, the high transmission is achieved over 70% in the same desired transmission region as mentioned above. In conclusion, we finally obtain the splitter–combiner whose high transmission region ranges from 1539.4 nm to 1561.7 nm, which corresponds to the expected wavelength region in which we are interested in the slow light waveguide section. Fig. 7(a) and (b) shows the simulation results of the TE-polarized light propagation through the structure as splitter and combiner with really low loss, respectively. The FDTD simulation results support our analysis of the high transmission mechanism.

4.3. Design of the whole structure

Based on the analysis above, we have successfully achieved three parts of the MZI modulator. However, integrating the three parts together remains a challenge, because of the poor transmission properties resulting from the mismatch between the two modes. Recently, kinds of structures have been studied to solve this problem

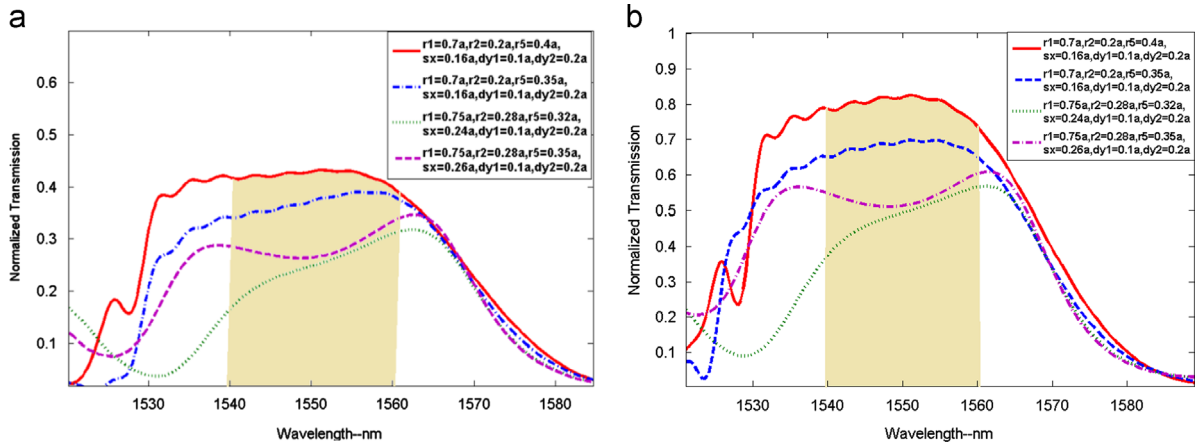

Fig. 6. (a) Transmission spectrum of the structure operating as splitter when the parameters of the numbered holes vary. (b) Transmission spectrum of the structure operating as combiner when the parameters of the numbered holes vary.

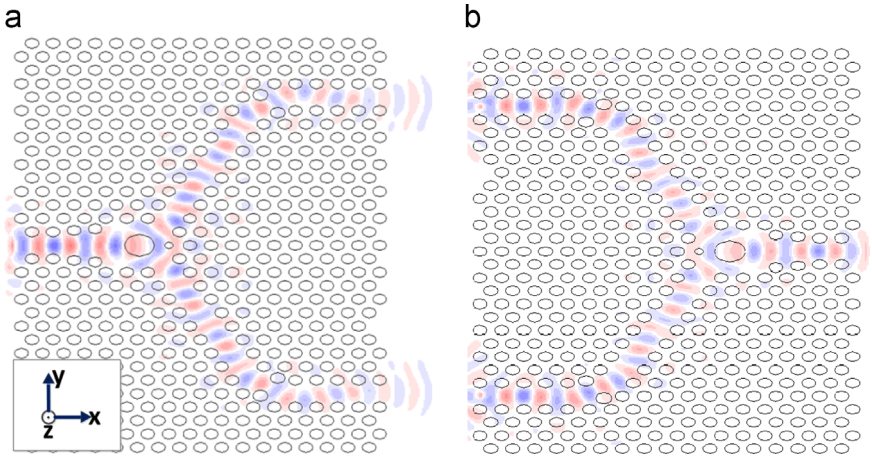

Fig. 7. (a) Steady state electric field profile for the TE-polarized wave propagating through propagation through the optimized structure as a splitter with the operating frequency $w_0 = 0.416(2\pi c/a)$. (b) Steady state electric field profile for the TE-polarized wave propagating through propagation through the optimized structure for combining with the operating frequency $w_0 = 0.416(2\pi c/a)$.

[36–38]. Here we present the simulation of a coupling device made from a PC step taper, which significantly increases the transmission properties of the integrated MZI modulator.

In order to numerically investigate the efficiencies of different couplers with different lengths and position shifts, we simulate transmission through a structure consisting of simple PC line defect waveguide with $r = 0.32a$ and 13 periods slow light waveguide designed before. The length of the slow light section is chosen to be 13 periods for the reason that the transmission spectrum becomes independent of the number of periods in that way. The schematic configuration of the step taper is shown in Fig. 2. As Fig. 8 shows, we calculate how the length of the step taper and $S1$ have an influence on the coupling efficiency. We can figure out that when the length of the step taper is no more than 8 periods, the coupling efficiency increases along with the increase of the length. And when the length of the taper is fixed, the coupling efficiency increases along with the increase of $S1$. After a careful design we choose the parameters to be $n = 8a$, and $S1 = 0.25a$ and the coupling efficiency is shown by the red line in Fig. 8. And the coupling efficiency is over 50% in the desired low dispersion region. It is clear that the coupling efficiency is chiefly improved from 1539.4 nm to 1561.7 nm, which is the slowdown region we are concerned about.

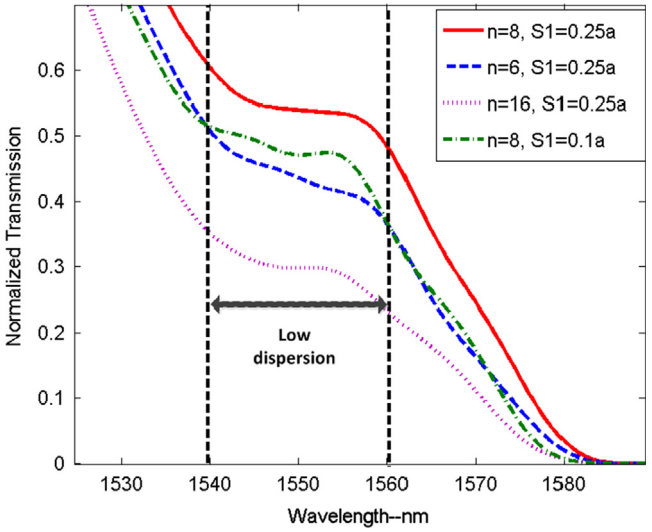

Fig. 8. Transmission spectrum of the optimized PC step taper with different length or different $S1$. $S1$ means the position shift of the first line of the step taper and n is the length of the step taper.

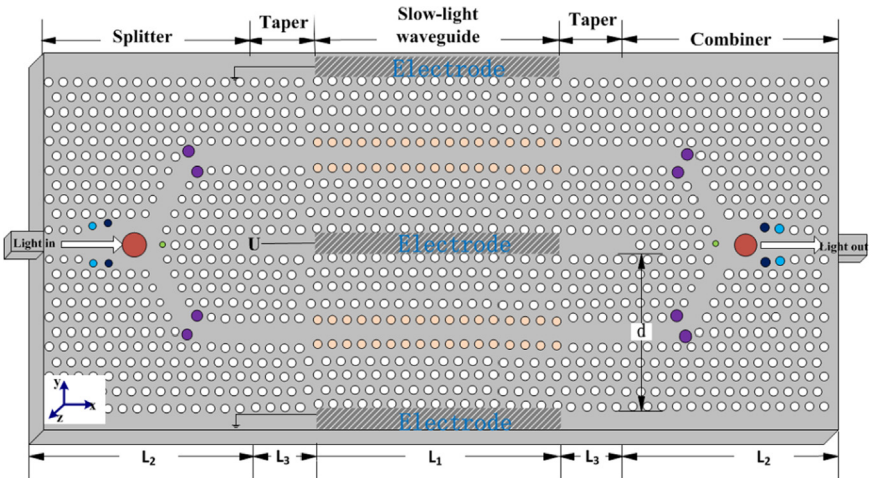

Fig. 9. Schematic of the optimized MZI modulator.

Table 2
Characteristic data for a PC MZI modulator when the modulation bandwidth is fixed at $f_{3\ \mathrm{db}}=100$ GHz.

a (nm)	L (μm)	d (μm)	n_g	$f_{3\ \mathrm{dB}}$ (GHz)	W (nm)	U_π (v)
646	138.24	4.51	17	99.6	29.6	3.53
645	91.59	4.50	27.5	100.8	22.3	2.64
634	71.64	4.42	37	100.3	15.1	2.29
627	68.34	4.37	44	100.1	11.6	2.07
623	61.05	4.25	45	99.8	8.0	2.05

Table 3
Characteristic data for a PC MZI modulator when the modulation bandwidth is fixed at $f_{3\ \mathrm{db}}=60$ GHz.

a (nm)	L (μm)	d (μm)	n_g	$f_{3\ \mathrm{dB}}$ (GHz)	W (nm)	U_π (v)
646	187.04	4.51	17	59.78	29.6	2.12
645	129.64	4.50	27.5	60.09	22.3	1.63
634	105.24	4.42	37	59.69	15.1	1.36
627	93.42	3.73	44	59.71	11.6	1.23
623	91.58	4.25	45	60.03	8.0	1.19

5. Analysis of the MZI modulator's performance

The configuration of the MZI modulator optimized is shown schematically in Fig. 9. And the final designed modulator consists of four parts: the splitter, combiner, slow light waveguide and step taper. According to the analysis above, the MZI modulator can work over the wavelength 1539.4 – 1561.7 nm. The transmission spectrum of the optimized photonic crystal MZI modulator with the operating frequency of $w_0=0.416(2\pi c/a)$ is shown clearly in Fig. 10. It is obvious that the light is efficiently coupled in and out of the slow light waveguide and the transmission of the modulator is improved. In other words, we have successfully achieved a monolithic photonic crystal MZI modulator.

We also discuss the performance of the optimized MZI modulator, such as the half-wave voltage, modulation bandwidth, device size, and available bandwidth. The linear electro-optic coefficient γ_{33} of $LiNbO_3$ is supposed to be 30.9×10^{-12} m/V and the extraordinary refractive index of $LiNbO_3$ is 2.143(n_{LN}) [16]. Based on Eqs. (6), (8) and (10), we display our design based on the other two sets of simulated results about the slow light waveguide in Tables 2 and 3. The lattice constant a, local field factor f_{opt}, group refractive index n_g, modulated bandwidth $f_{3\ \mathrm{dB}}$, and slow light bandwidth W are calculated in the communication wavelength 1550 nm.

As shown in Tables 2 and 3, when the group index n_g increases, the length L modulation voltage U_π, and the available bandwidth decrease. We find that the available bandwidth decreases more obviously than modulation voltage U_π and the two parameters have much more influence on the application of the modulator. Furthermore, with the purpose of avoiding having different MZI modulators operating at each optical wavelength, it is necessary to maintain modulator coverage over a large optical bandwidth. Thus we prefer to the one with higher bandwidth. From Tables 2 and 3, it is clear that for fixing the modulation bandwidth of $f_{3\ \mathrm{dB}}=100$ GHz, we achieve a structure of only $L=91.59\ \mu m$ and a small half driving voltage$U=U_\pi/4=0.66$ V. While fixing the modulation bandwidth of $f_{3\ \mathrm{dB}}=60$ GHz, it is possible to attain a structure of $L=129.64\ \mu m$ and a small half driving voltage of $U=U_\pi/4=0.41$ V. And the device can be applied to the 60 GHz system such as the ROF system. Meanwhile, we can figure out that slow light modulator can cover over 22.3 nmoptical bandwidth, so that the slow light modulator can be employed more widely. In our design, we achieve a MZI electro-optic modulator on one monolithic photonic crystal integrated structure. And the structure which covers over a large bandwidth combines the ultra-compact size, low driving voltage and high modulation bandwidth.

In order to investigate the designed modulator further, we study the characteristics of the pulses in the 100 GHz MZI modulator by time-domain simulation when different voltages are applied. At the input of our MZI modulator, we launch a pulse with a Gaussian frequency profile, a carrier frequency of $w_0=0.416(2\pi c/a)$, and a FWHM of $\Delta w/w_0=1/500$. During the simulations, we monitor the electric field $E(t)$ at end of the two arms of the modulator. According to expression (5), when the applied voltage is 0 V, 0.66 V, and 1.32 V, the refractive index change $|\Delta n|$ is 0, 0.00331, 0.00662 respectively, and the phase differences of the two arms of the modulator are 0, $\pi/2$, and π respectively based on expression (7).

When the applied voltage is 0 V, there is no refractive index change, and the simulation result is shown in Fig. 11. As shown in Fig. 11(b), it is clear that there is no phase difference between the pulse in the upper arm and the pulse in the lower arm. Next we change the refractive index to $n_{LN}-|\Delta n|$ in the upper arm in the slow light region of the modulator, and refractive index to $n_{LN}+|\Delta n|$ in the lower arm in the slow light region of the modulator. When $|\Delta n|$ is 0.00331, the corresponding applied voltage is 0.66 V, and the simulation result is shown in Fig. 12. It is obvious that the phase difference between the pulse in the upper arm and the pulse in the lower arm is $\pi/2$ in Fig. 12(b). If $|\Delta n|$ is 0.00662 and the corresponding voltage is 1.32 V, the simulation

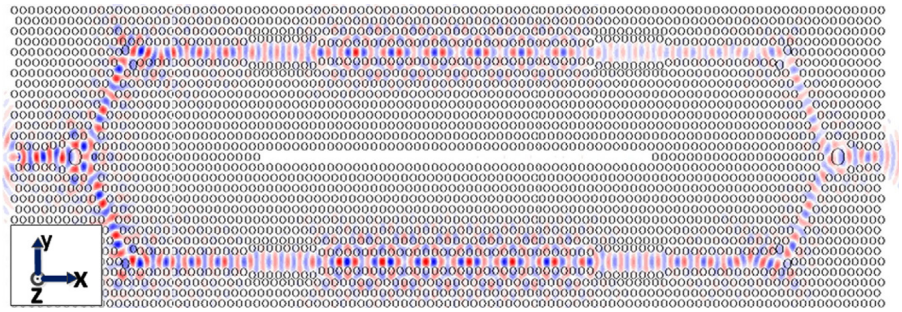

Fig. 10. Steady state electric field profile for the TE-polarized propagating through MZI modulator.

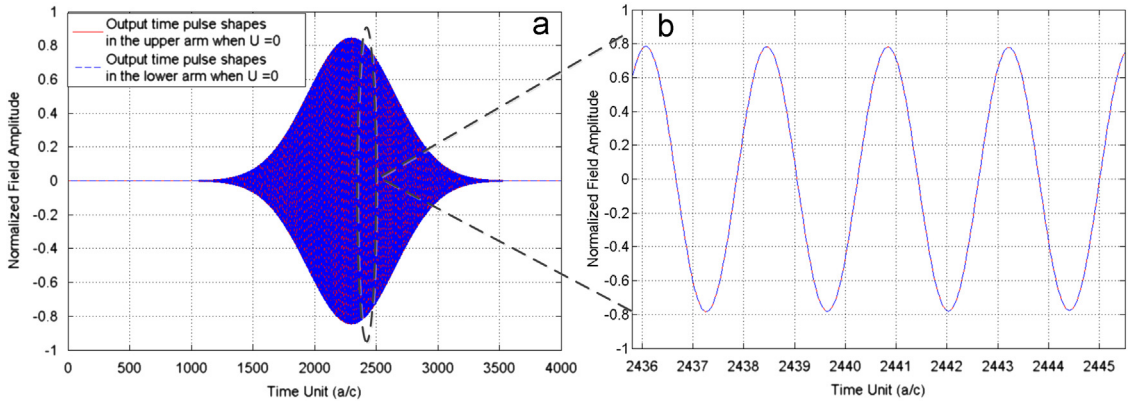

Fig. 11. (a) The electiec field is plotted as a function of time.The red and the blue signals represent the output pulses in the upper and lower arms of the modulator respectively when applied voltage is $U = U_{\pi}/4 = 0$ V. (b) The red and the blue signals represent the detail of the output pulses in the upper and lower arms of the modulator respectively. (For interpretation of the references to color in this figure legend, the reader is referred to the web version of this article.)

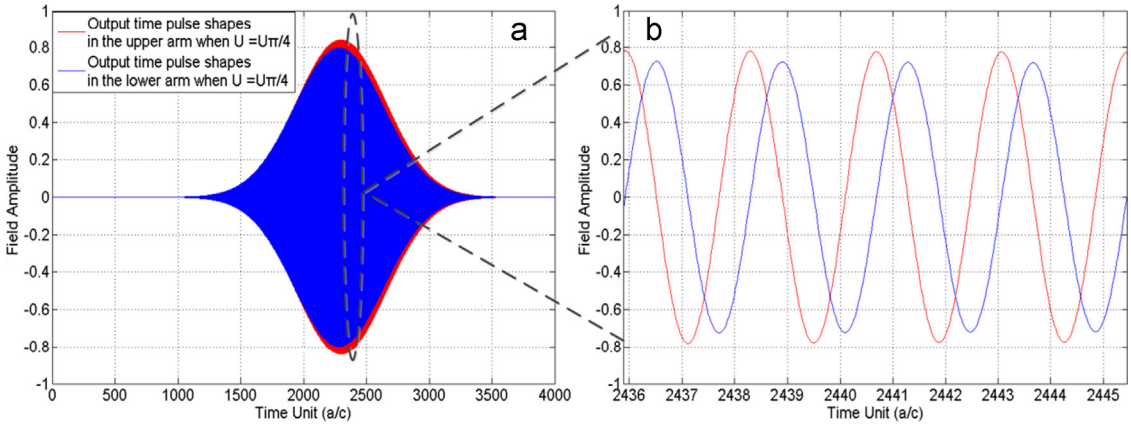

Fig. 12. (a) The electiec field is plotted as a function of time.The red and the blue signals represent the output pulses in the upper and lower arms of the modulator respectively when applied voltage is $U = U_{\pi}/4 = 0.66$ V. (b) The red and the blue signals represent the detail of the output pulses in the upper and lower arms of the modulator respectively. (For interpretation of the references to color in this figure legend, the reader is referred to the web version of this article.)

result is shown in Fig. 13. We can note that the phase difference is π in Fig. 13(b). Meanwhile, we also monitor the electric field squared $|E|^2$ at output end of the modulator, and the simulation result is shown in Fig. 14. We can note that when $U = U_{\pi}/4$ is applied, the output light intensity is nearly half of the output light intensity without applied voltage, which agrees with the transmission curve of MZI electro-optic modulator when the phase difference between the two arms is $\pi/2$.

Next we study the optical losses of the designed modulator according to the way used in [40]. Fig. 14 shows the transmission characteristics of the designed modulator. The transmission data is normalized to the output spectrum of the modulator. Our result indicates that the optical loss over the low dispersion bandwidth (1539.4 − 1561.7 nm) is 5.1 ± 0.8 dB, which includes optical loss from the slow light crystal, propagation loss from the material and the mental electrodes and the loss in the splitter–combiner. The simulation results in Section 4 indicate that the optical loss in the splitter–combiner is 2.1 dB and the optical loss in the slow light waveguides (including couplers) is 2.6 dB. From the data mentioned above, one can see that the losses are mainly from the

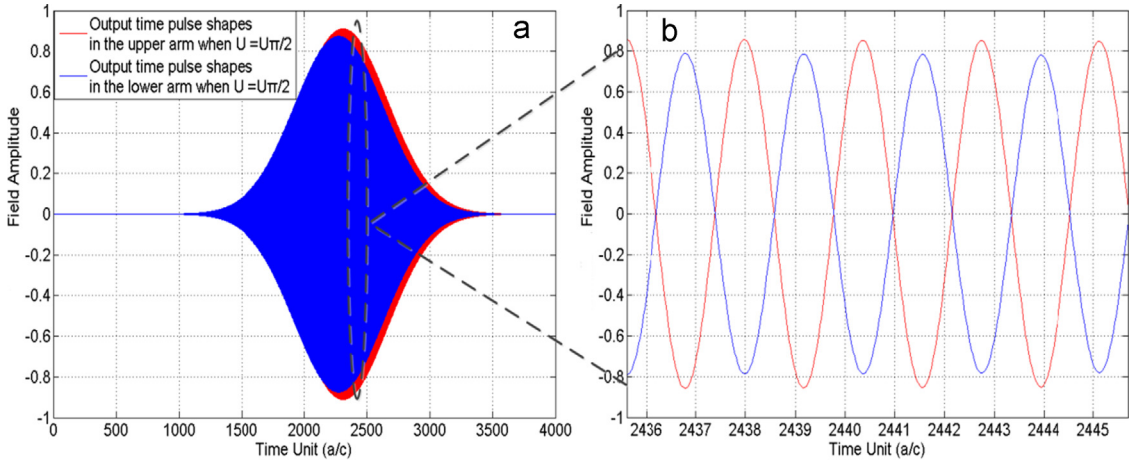

Fig. 13. (a) The electiec field is plotted as a function of time.The red and the blue signals represent the output pulses in the upper and lower arms of the modulator respectively when applied voltage is $U = U_{\pi}/4 = 1.32$ V. (b) The red and the blue signals represent the detail of the output pulses in the upper and lower arms of the modulator respectively. (For interpretation of the references to color in this figure legend, the reader is referred to the web version of this article.)

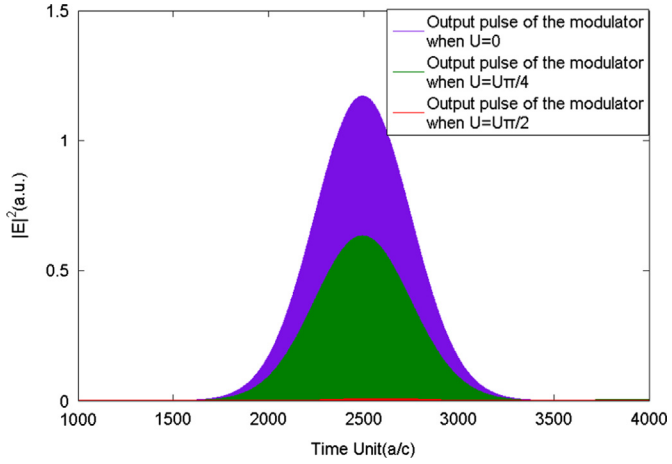

Fig. 14. The electiec field squared is plotted as a function of time,observrd at the output end of the modulator when different voltage U is appled to the modulator.

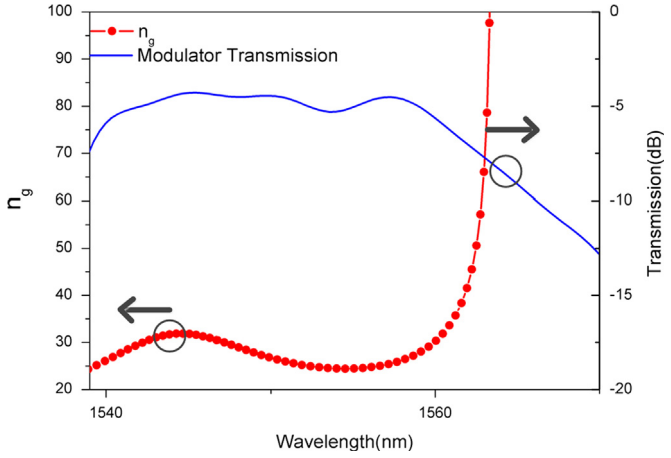

Fig. 15. Transmission spectrum of the MZI modulator (blue curve) and the calculated group index (red curve). (For interpretation of the references to color in this figure legend, the reader is referred to the web version of this article.)

optical losses which are from the slow light crystal, propagation losses from the material and the losses in the splitter–combiner (Fig. 15).

6. Conclusion

In this paper, we study a slow light MZI electro-optic modulator in theory. The modulator is firstly studied on a monolithic photonic crystal integrated chip by simulation. The modulator consists of four parts: the splitter, combiner, slow light waveguides and step tapers. With optimization, these parts are integrated on the same photonic crystal chip with high performance to realize the function of modulating. The group index is achieved to be $n_g = 27.5$. The transmission of the splitter is above 40% (each output) and the transmission of the combiner is above 70%. With the step taper, the coupling efficiency is highly enhanced and the transmission of the modulator is highly improved. Finally, we have successfully combined the ultra-compact size, low driving voltage and high modulation bandwidth for the structure which is of a drive voltage of 0.66 V, a bandwidth of 100 GHz and a size of $L = 91.59\ \mu m$. Meanwhile, the structure can also be designed with a drive voltage of 0.41 V, and a size of $L = 129.64\ \mu m$ which can work on the modulation bandwidth of 60 GHz. And the modulator covers over 22.3 nm optical bandwidth at telecom wavelength range. The proposed structure is promising and potent for device integration especially for those based on photonic crystal in theory.

Acknowledgments

This research was supported in part by National 973 Program (No. 2012CB315705), Project 61372038 supported by NSFC, National 863 Program (No. 2011AA010303), and Fund of State Key Laboratory of Information Photonics and Optical Communications (Beijing University of Posts and Telecommunications), PR China. Thanks for the great help.

References

[1] William M.J. Green, Michael J. Rooks, Lidija Sekaric, Yurii A. Vlasov, Opt. Express 15 (2007) 17106.
[2] Peter Horvath, Istvan Frigyes, IEEE Commun. Lett. 9 (2005) 921.
[3] Ansheng Liu, Ling Liao, Doron Rubin, Opt. Express 15 (2007) 660.
[4] Ling Liao, Dean Samara-Rubio, Michael Morse, Ansheng Liu, Dexter Hodge, Opt. Express 13 (2005) 3129.
[5] L. Alloatti, D. Korn, R. Palmer, D. Hillerkuss, J. Li, A. Barklund, R. Dinu, J. Wieland, M. Fournier, J. Fedeli, H. Yu, W. Bogaerts, P. Dumon, R. Baets, C. Koos, W. Freude, J. Leuthold, Opt. Express 19 (2011) 11841.
[6] Jan Hendrik Wülbern, Stefan Prorok, Jan Hampe, Opt. Lett. 35 (2010) 2753.

[7] Bartos Chmielak, Michael Waldow, Christopher Matheisen, Christian Ripperda, Jens Bolten, Thorsten Wahlbrink, Michael Nage, Florian Merget, Heinrich Kurz, Opt. Express 19 (2011) 17212.
[8] Melissa Ziebell, Delphine Marris-Morini, Gilles Rasigade, Jean-Marc Fédéli, Paul Crozat, Eric Cassan, David Bouville, Laurent Vivien, Opt. Express 20 (2012) 10591.
[9] Jianfeng Ding, Hongtao Chen, Lin Yang, Lei Zhang, Ruiqiang Ji, Yonghui Tian, Weiwei Zhu, Yangyang Lu, Ping Zhou, Rui Min, Mingbin Yu, Opt. Express 20 (2012) 7081.
[10] Jianfeng Ding, Hongtao Chen, Lin Yang, Lei Zhang, Ruiqiang Ji, Yonghui Tian, Weiwei Zhu, Yangyang Lu, Ping Zhou, Rui Min, Opt. Express 20 (2012) 3209.
[11] Luca Terlevich, Stefano Balsamo, Simone Pensa, Marco Pirola, Giovanni Ghione, J. Lightwave Technol. 24 (6) (2006) 2355.
[12] B.M. Azizur Rahman, V. Haxha, S. Haxha, K.T.V. Grattan, J. Lightwave Technol. 24 (2006) 3506.
[13] Maria Morant, Roberto Llorente, Jerome Hauden, Terence Quinlan, Alexandre Mottet, Stuart Walker, Opt. Express 19 (2011) B450.
[14] Kensuke Ogawa, Kazuhiro Goi, Yong Tsong Tan, Tsung-Yang Liow, Xiaoguang Tu, Qing Fang, Guo-Qiang Lo, Dim-Lee Kwong, Opt. Express 19 (2011) B26.
[15] Hong C. Nguyen, Yuya Sakai, Mizuki Shinkawa, Opt. Express 19 (2011) 13000.
[16] Jan-Michael Brosi, Christian Koos, Lucio Claudio Andreani, Michael Waldow, Juerg Leuthold, Wolfgang Freude, Opt. Express 16 (2008) 4177.
[17] Xueying Wang, Huiping Tian, Yuefeng Ji, J. Opt. 12 (2010) 1–4.
[18] Sara Bakhshi, Mohammad Kazem Moravvej-Farshi, Majid Ebnali-Heidari, Appl. Opt. 51 (2012) 2687.
[19] Daquan Yang, Huiping Tian, Yuefeng Ji, Opt. Express 19 (2011) 20023.
[20] Yi Zhai, Huiping Tian, Yuefeng Ji, J. Lightwave Technol. 29 (2011) 3083.
[21] Jasmin Smajic, Christian Hafner, Daniel Erni, Opt. Express 11 (2003) 1378.
[22] L.H. Frandsen, P.I. Borel, Y.X. Zhuang, Opt. Lett. 29 (2004) 1623.
[23] Jian-Hua Chen, Yang-Tung Huang, Yu-Lin Yang, Ming-Feng Lu, Jia-Min Shieh, Appl. Opt. 51 (2012) 5876.
[24] Huihui Lu, Fadi Issam Baida, Gwenn Ulliac, Nadège Courjal, Manuel Collet, et al., Appl. Phys. Lett. 101 (2012) 151117.
[25] M.-P. Bernal, J. Amet, J. Safioui, F. Devaux, M. Chauvet, et al., Appl. Phys. Lett. 98 (2011) 071101.
[26] Y.R. Shen, The Principles of Nonlinear Optics, Wiley, New York, 1984; R.W. Boyd, Nonlinear Optics, Academic, New York, 2003.
[27] R. Frey, P. Delaye, G. Roosen, Nanophotonique, in: J-M. Lourtioz, C. Delalande, A. Levenson, H. Rigneault (Eds.), Hermès-Lavoisier, Paris, 2005.
[28] H. Lu, B. Sadani, G. Ulliac, N. Courjal, C. Guyot, J.-M. Merolla, M. Collet, F.I. Baida, M.-P. Bernal, Opt. Express 20 (2012) 20884.
[29] H. Lu, B. Sadani, G. Ulliac, N. Courjal, C. Guyot, J.-M. Merolla, M. Collet, F.I. Baida,and, M.-P. Bernal, Opt. Express 20 (2012) 2974.
[30] M. Roussey, M.-P. Bernal, N. Courjal, D. Van Labeke, F.I. Baida, Appl. Phys. Lett. 89 (2006) 241110.
[31] Matthieu Roussey, Fadi I. Baida, Maria-Pilar Bernal, J. Opt. Soc. Am. B 24 (2007) 1416.
[32] J. Amet, G. Ulliac, F.I. Baida, M.-P. Bernal, Appl. Phys. Lett. 96 (2010) 103111.
[33] Toshihiko Baba, Takashi Kawasaki, Hirokazu Sasaki, Jun Adachi, Daisuke Mori, Opt. Express 16 (2008) 9245.
[34] Guansheng Shen, Huiping Tian, Yuefeng Ji, Appl. Opt. 52 (2013) 1218.
[35] Shousaku Kubo, Daisuke Mori, Toshihiko Baba, Opt. Lett. 32 (2007) 2981.
[36] S. Boscolo, M. Midrio, Opt. Lett. 27 (2002) 1001.
[37] Woo Jun Kim, John D. O'Brien, J. Opt. Soc. Am. B 21 (2004) 289.
[38] Ming-Feng Lu, Shan-Mei Liao, Yang-Tung Huang, Appl. Opt. 49 (2010) 724.
[39] Hung-Ta Chien, Chengkuo Lee, Hua-Kung Chiu, Kuei-Chu Hsu, Chii-Chang Chen, Ja-an Annie Ho, Chien Chou, J. Lightwave Technol. 27 (2009) 2570.
[40] Somayyeh Rahimi, Amir Hosseini, Xiaochuan Xu, Harish Subbaraman, Ray T. Chen, Opt. Express 19 (2011) 21832.
[41] Amir Hosseini, Xiaochuan Xu, David N. Kwong, Harish Subbaraman, Wei Jiang, Ray T. Chen, Appl. Phys. Lett. 98 (2011) 031107-1.
[42] Alejandro Martinez, Pablosanchi Javier Marti, Opt. Quantum Electron. 37 (2005) 77.
[43] S. Olivier, H. Benisty, C. Weisbuch, C.J.M. Smith, T.F. Krauss, R. Houdré, U. Oesterle, J. Lightwave Technol. 20 (2002) 1198.